Space Sci Rev (2016) 199:105–135
DOI 10.1007/s11214-014-0109-8

The FIELDS Instrument Suite on MMS: Scientific Objectives, Measurements, and Data Products

R.B. Torbert · C.T. Russell · W. Magnes · R.E. Ergun · P.-A. Lindqvist · O. LeContel · H. Vaith · J. Macri · S. Myers · D. Rau · J. Needell · B. King · M. Granoff · M. Chutter · I. Dors · G. Olsson · Y.V. Khotyaintsev · A. Eriksson · C.A. Kletzing · S. Bounds · B. Anderson · W. Baumjohann · M. Steller · K. Bromund · Guan Le · R. Nakamura · R.J. Strangeway · H.K. Leinweber · S. Tucker · J. Westfall · D. Fischer · F. Plaschke · J. Porter · K. Lappalainen

Received: 14 May 2014 / Accepted: 16 October 2014 / Published online: 19 November 2014

R.B. Torbert (✉) · O. LeContel · H. Vaith · J. Macri · S. Myers · D. Rau · J. Needell · B. King · M. Granoff · M. Chutter · I. Dors
University of New Hampshire, Durham, NH, USA
e-mail: roy.torbert@unh.edu

G. Olsson
Royal Institute of Technology, Stockholm, Sweden

Y.V. Khotyaintsev · A. Eriksson
Swedish Institute of Space Physics, Uppsala, Sweden

J. Porter · K. Lappalainen
University of Oulu, Oulu, Finland

R.E. Ergun · S. Tucker · J. Westfall
University of Colorado, Boulder, CO, USA

R.B. Torbert
Southwest Research Institute, San Antonio, TX, USA

C.T. Russell · R.J. Strangeway · H.K. Leinweber
University of California, Los Angeles, CA, USA

K. Bromund · G. Le
NASA Goddard Space Flight Center, Greenbelt, MD, USA

C.A. Kletzing · S. Bounds
University of Iowa, Iowa City, IA, USA

B. Anderson
Johns Hopkins Applied Physics Laboratory, Laurel, MD, USA

W. Magnes · W. Baumjohann · M. Steller · R. Nakamura · D. Fischer · F. Plaschke
Space Research Institute, Austrian Academy of Sciences, Graz, Austria

P.-A. Lindqvist
Laboratory for Plasma Physics, Paris, France

Abstract The FIELDS instrumentation suite on the Magnetospheric Multiscale (MMS) mission provides comprehensive measurements of the full vector magnetic and electric fields in the reconnection regions investigated by MMS, including the dayside magnetopause and the night-side magnetotail acceleration regions out to 25 Re. Six sensors on each of the four MMS spacecraft provide overlapping measurements of these fields with sensitive cross-calibrations both before and after launch. The FIELDS magnetic sensors consist of redundant flux-gate magnetometers (AFG and DFG) over the frequency range from DC to 64 Hz, a search coil magnetometer (SCM) providing AC measurements over the full whistler mode spectrum expected to be seen on MMS, and an Electron Drift Instrument (EDI) that calibrates offsets for the magnetometers. The FIELDS three-axis electric field measurements are provided by two sets of biased double-probe sensors (SDP and ADP) operating in a highly symmetric spacecraft environment to reduce significantly electrostatic errors. These sensors are complemented with the EDI electric measurements that are free from all local spacecraft perturbations. Cross-calibrated vector electric field measurements are thus produced from DC to 100 kHz, well beyond the upper hybrid resonance whose frequency provides an accurate determination of the local electron density. Due to its very large geometric factor, EDI also provides very high time resolution ($\sim$ 1 ms) ambient electron flux measurements at a few selected energies near 1 keV. This paper provides an overview of the FIELDS suite, its science objectives and measurement requirements, and its performance as verified in calibration and cross-calibration procedures that result in anticipated errors less than 0.1 nT in **B** and 0.5 mV/m in **E**. Summaries of data products that result from FIELDS are also described, as well as algorithms for cross-calibration. Details of the design and performance characteristics of AFG/DFG, SCM, ADP, SDP, and EDI are provided in five companion papers.

Keywords Magnetic reconnection · Magnetospheric dynamics · Magnetospheric multiscale · Electromagnetic field measurements

1 Introduction

The paradigm of magnetic reconnection has been one of the central organizing principles of space physics since it was first comprehensively used by Dungey (1953) to explain explosive space plasma phenomena such as magnetic storms and solar flares, although suggestions of the principles of reconnection were put forward earlier by Giovanelli (1946), Hoyle (1949), and Cowling (1953). Theories of the process were put forward by Sweet and Parker (1957, 1963) that led to the conclusion that conventional MHD processes were much too slow to accommodate the explosive events that are attributed to reconnection. An alternative theory by Petschek (1964) seemed to have resolved this issue with the inclusion of MHD shocks, which, however, were never conclusively observed in the extensive observations around the Earth's dayside magnetopause and magnetotail, regions where Dungey had suggested reconnection must take place and which were accessible to in-situ measurement with spacecraft. Nevertheless, an extensive body of observational evidence has been accumulated with spacecraft such as ISEE, AMPTE, Polar, Wind, Cluster and THEMIS that lead to the present scientific consensus that reconnection is surely taking place in these regions, and other astrophysical settings as well, but that no clear understanding of its underlying mechanism is manifest. As of this writing, neither observations nor theory have enough fidelity to pinpoint this mechanism, or mechanisms.

The general picture that has remained valid since Dungey (at least for two-dimensional reconnection where opposing magnetic fields are anti-parallel) is sketched in Fig. 1 (Mozer

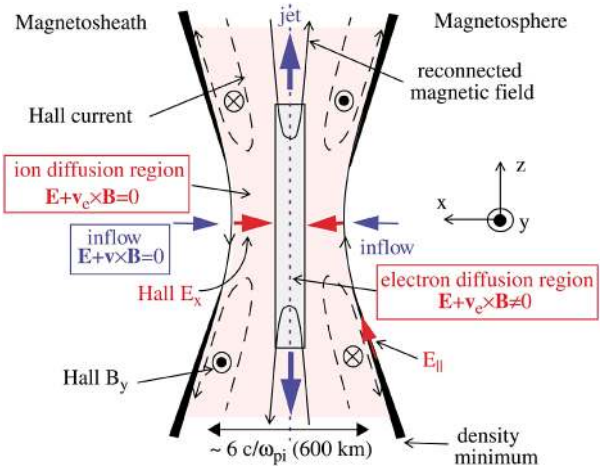

Fig. 1 Two-dimensional reconnection topology

et al. 2002). The anti-parallel primary magnetic field in the z direction is embedded in the plasma which flows with an $\mathbf{E} \times \mathbf{B}$ or "frozen in" velocity, and transports magnetic flux in opposing x directions under the influence of the reconnection electric field, in the y direction normal to the page. This field is converted into mechanical energy that accelerates the plasma in jets of z-directed velocity with speeds of order the Alfvén speed of the incoming plasma. Observations have confirmed the suggestions of Sonnerup (1984) and others that a scale separation is established due to the different inertia of ions and electrons, whereby the ions are accelerated and do not flow with a $\mathbf{E} \times \mathbf{B}$ velocity over a region of size $d_i = c/\omega_{pi}$ whereas the electrons remain frozen in until a much smaller scale region is encountered, of size c/ω_{pe}. This separation is the effect of the Hall $\mathbf{J} \times \mathbf{B}$ term in the generalized Ohm's law for plasmas:

$$\mathbf{E} + \mathbf{U} \times \mathbf{B} = \eta \mathbf{J} + \frac{1}{en}\mathbf{J} \times \mathbf{B} - \frac{1}{en}\nabla \cdot \overleftrightarrow{\mathbf{P}_e} + \frac{m_e}{n_{e^2}}\frac{\partial \mathbf{J}}{\partial t} \tag{1}$$

where η is the resistivity (presumably anomalous, due to high frequency plasma waves) and $\mathbf{P}_e$ is the electron pressure tensor. The Hall separation establishes a perpendicular electric field, E_x, and a perturbation magnetic field, B_y, that results in an observed quadrupolar magnetic signature on the scale size of the of ion diffusion region. However, the relative contributions of the Hall term to those of others in Ohm's law that give rise to dissipation and energy conversion, the inertial term, the pressure term, and the resistivity term (which for collisionless plasmas is mainly due to anomalous resistivity from wave action) is a matter of hot debate in both the observational and theoretical literature. In particular, the role of the electric field parallel to the magnetic field, which cannot be driven by the Hall term, is not clear.

The observational situation can be exemplified by the data from the Cluster 4 spacecraft seen in Fig. 2 (Andre et al. 2004). These data are taken in a thin ($\sim$ 20 km) current layer near the dayside magnetopause with the highest time resolution available to Cluster. This current layer exists on the magnetospheric side of the magnetopause and cannot be identified by the authors as *the* electron diffusion region, although it is of the size of the electron inertial length (4 km), but is probably the signature of a separatrix that extends from such a region. The layer can be seen in the magnetic field data of panel (e) and the estimated currents of panel (f), extending over approximately one second. There are 50 mV/m perpendicular electric fields seen in panel (c), which agree with the estimate of the $\mathbf{J} \times \mathbf{B}$ term in Eq. (1), using

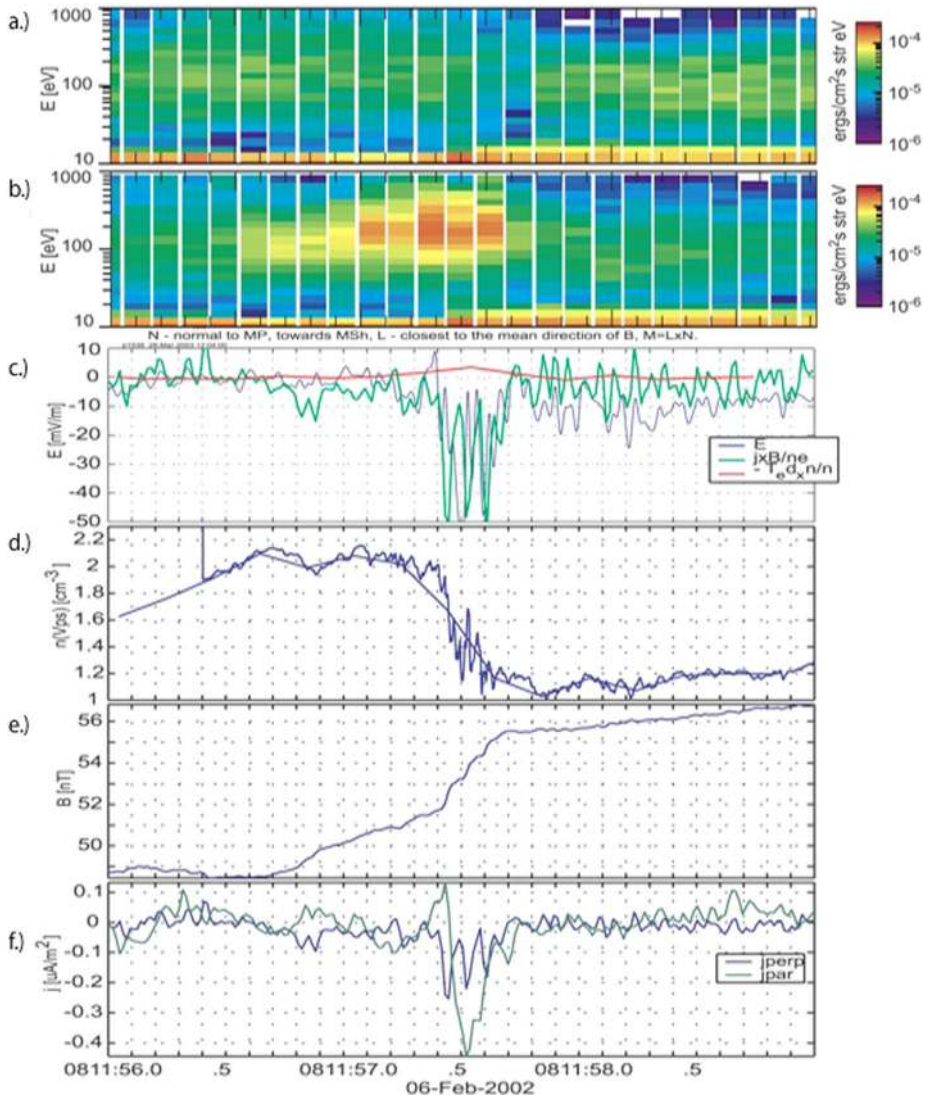

Fig. 2 Cluster encounter with thin reconnection current sheet

the currents in panel (f) estimated from the single satellite magnetic field profile (essentially, dB/(vdt)). Thus, this electric field may be predominately a Hall electric field. Panels (a) and (b) are spectra of electrons at velocities nearly perpendicular and parallel, respectively, to the magnetic field. As the directions of these fluxes are changing as the satellite spins with a period of 4 seconds, a full distribution function cannot be determined for either electrons or ions, but the data in panels (b) and (f) indicate that a parallel current is present, carried by ~ 150 eV electrons.

The red line of panel (c) is a proxy for the pressure term of Eq. (1), and would suggest that this term is not important for this reconnection event. However, the full evaluation of this term is not possible with previous satellite instrumentation, including that for Cluster, and

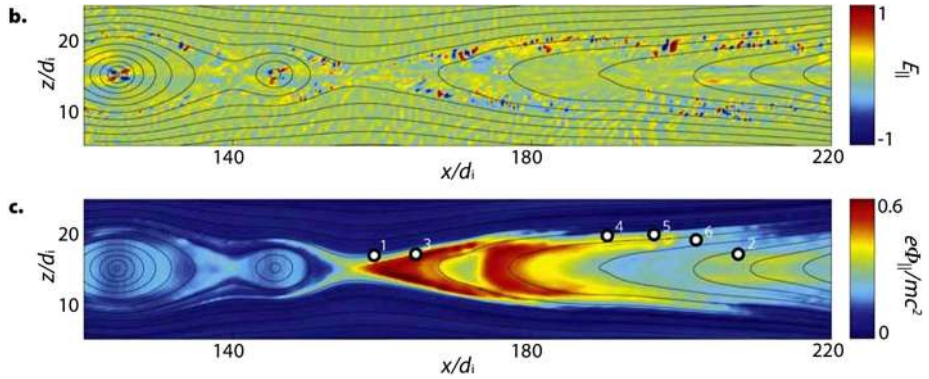

Fig. 3 Simulation results for **E** parallel to **B** (Egedal et al. 2012)

this result is open to question. Cluster cannot determine the important parallel component of the electric field, except in very rare current sheet orientations, because there were no 3-axis sensors for this mission. The authors also confirm that the pressure terms and the inertial term, which would correspond to a parallel electric field, are impossible to determine from the time and energy resolution available with Cluster instrumentation, nor is there sufficient ion flux resolution to determine the $\mathbf{U} \times \mathbf{B}$ term in Ohm's law on these time scales. Thus, although this observation hints at intriguing reconnection dynamics occurring on the scale size of the electron diffusion region, the important discriminating mechanisms for the reconnection process are undetermined.

Because satellites are capable of sampling only one or a few points (four, in the case of Cluster and MMS), in-situ measurements have been supplemented with more and more sophisticated plasma simulations. In fact, MMS has a resident theory and modeling team (see Hesse et al. 2014, this issue) to provide models that are tailored to the experimental conditions that MMS may experience. At this time, these simulations are limited in their approximations to the quite complex plasmas that surround reconnection regions, and there are controversial and divergent opinions between various simulations as to the critical characteristics of reconnection. The example of the role of the parallel electric field serves to illustrate this situation.

Figure 3 shows the parallel electric field and an estimate of the potential along the field line from a simulation by Egedal et al. (2012). The authors claim that the significant energization of electrons that has been observed in reconnection can be attributed to the parallel acceleration seen here all along the separatrix of the primary x-point (at $\sim 155 d_i$), but there is very little parallel field near that x-point. Pritchett and Mozer (2009) report a simulation (see Fig. 4) that also has no parallel signature right at the x-point, but closely surrounding it and with a different spatial distribution of the field. If the curl of the field is non-zero surrounding the diffusion region, it will contribute importantly to non-frozen-in electron flow, but the total electron energization may be significantly less than that seen in the simulation by Egedal. Nearly all discussions like these agree that the parallel electric field is a critical parameter in reconnection, but may differ widely regarding both the contribution of that field and also the spatial characteristics of the field amplitude around diffusion regions. For example, Drake (2010) reports other simulations that attribute the electron energy gain to Fermi-like acceleration between rapidly fluctuating magnetic islands. An accurate measurement of the parallel electric field is one of the major goals of the MMS FIELDS suite, as its

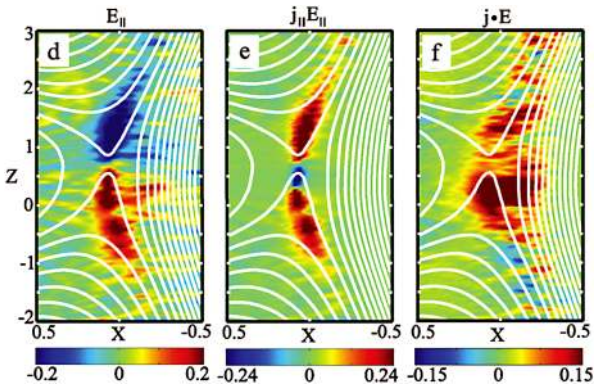

Fig. 4 Topologies of fields and related quantities for asymmetric reconnection with no guide field (Pritchett and Mozer 2009)

magnitude and distribution will discriminate among competing theories and simulations of reconnection.

2 Science Objectives and Requirements

The importance of the reconnection process lies in the fact that it is the universal process by which magnetic energy is transferred to material particles in plasmas, as manifest in the solar wind's interaction with the Earth's magnetosphere, and in the explosive release of energy during substorms, solar flares, and high-energy astrophysical events. To resolve the questions remaining from previous missions and the extensive investigations of simulations of reconnection, the MMS mission was charged with three primary objectives: (1) understand the microphysics of magnetic reconnection by determining the kinetic processes occurring in the electron diffusion region that are responsible for collisionless magnetic reconnection, especially how reconnection is initiated; (2) determine the role played by electron inertial effects and turbulent dissipation in driving magnetic reconnection in the electron diffusion region; and (3) determine the rate of magnetic reconnection and the parameters that control it. The FIELDS suite provides data that is critical to achieving these objectives. Specifically, the FIELDS suite must resolve thin currents layers and magnetic fields within reconnection regions (and provide estimates of their gradients and curls with the use of multi-spacecraft observations), detect and identify plasma wave modes and characteristics; measure the decoupling of electrons from the magnetic field within the electron diffusion regions; determine the agents for energization of energetic electrons and ions; measure the 3D components of the reconnection electric field and, particularly, its parallel component.

As the name "magnetic reconnection" implies, MMS studies of reconnection require the precise measurement of the magnetic field, which is the source of the driving energy for reconnection. The magnetic field not only delineates the topology of connection and reveals the presence of current sheets where energy conversion occurs and electromagnetic waves that might produce that conversion, it also illuminates the geometry for particle motion and acceleration. The FIELDS suite measures the magnetic field with four independent sensors and provides algorithms for combining these four measurements into one precisely calibrated time series up to 16000 samples/s, sufficient to determine the role of the whistler mode in the kinetic physics of reconnection. The electric field determines energy conversion and particle acceleration within reconnection regions, and combined with the magnetic fields data, determines not only the frozen-in velocity, but also $\mathbf{J} \cdot \mathbf{E}$ and the waves that play

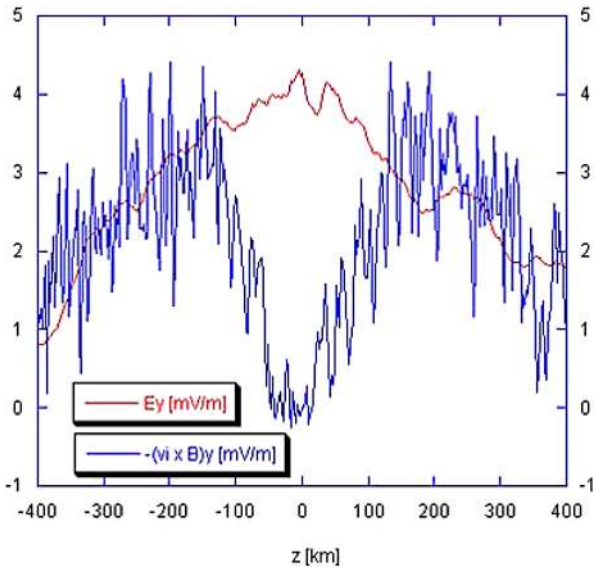

Fig. 5 Simulation results for non-frozen flow condition

a role in turbulent dissipation. The FIELDS suite encompasses three measurements of the electric field and again employs algorithms to combine these measurements to provide the first continuous, accurate determination of the 3D electric field. From this, the critical measurement of the parallel electric field can be deduced. Moreover, the magnetic and electric signatures seen by the MMS fleet as a whole are critical in determining the location of each of the satellites relative to reconnection structures such as those seen in Fig. 1.

The requirements on the electric and magnetic field sensors were determined by reference to the unmet needs of previous experimental studies as referenced above and to a series of simulations of the diffusion regions that were guided by such studies. For example, a signature of reconnection dissipation is the presence of a parallel electric field and a parallel current that are co-aligned ($\mathbf{J}_{par} \cdot \mathbf{E}_{par} > 0$) relative to the local magnetic field. Given that the Hall electric fields seen above were of order 50 to 100 mV/m, an angular error of 1 degree in the magnetic field direction, in diffusion regions where the magnitude of B may be 5–10 nT, implies an accuracy of no better that 1 mV/m on the parallel electric field. This may be the order of such a component in many places around reconnection sites. The one degree requirement in turn implies an accuracy of ~ 0.1 nT on each magnetic field component. For another perspective, Hesse (private communication) has simulated the terms in the left hand side of Eq. (1) above to determine the magnitude of the reconnection electric field component in the ion diffusion region, as seen in Fig. 5. To determine when $\mathbf{E}$ might be significantly different from the $-\mathbf{U} \times \mathbf{B}$, it is clear that an accuracy of order 1 mV/m is needed.

These studies led to the following requirements on the FIELDS suite:

(1) measure the vector DC magnetic field with accuracy of 0.1 nT every 10 ms.
(2) measure the vector (3D) DC electric field with accuracy better than 1 mV/m every 1 ms.
(3) measure plasma waves (electric vector to 100 kHz, magnetic vector to 6 kHz).

The first two of these requirements have proven to be very challenging in previous space plasma missions. The FIELDS suite meets these challenges by combining multiple sensors and multiple techniques that, in combination, are able to satisfy these demands.

3 Fields Suite Description

The above objectives are accomplished on MMS with six sensors integrated into the FIELDS suite, as diagrammed in Fig. 6 (institutional contributions indicated), with the control and data flow managed by the Central Electronics Box (CEB). The CEB also contains controllers for the Analog Flux Gate (AFG), Digital Flux Gate (DFG), and the Electron Drift Instrument (EDI) as well as the Digital Signal Processor (DSP) for the high frequency instruments of Search Coil Magnetometer (SCM), Spin-plane Double-Probes (SDP), and the Axial Double-Probes (ADP). Within the CEB, the Central Data Processing Unit (CDPU) coordinates all the functioning of the FIELDS suite, including power switching through the Low Voltage Power Supply (LVPS). The CDPU, LVPS, and DSP are all fully cold redundant. The CEB determines the synchronous timing regimen for the entire suite, all command processing, and can deliver up to 4 Mbps of data to the MMS spacecraft Central Instrument Data Processor (CIDP). Each of these sensors is described more completely in following companion papers, but this communication attempts to describe how they are all integrated together into one highly calibrated and cross-calibrated instrument suite to measure electromagnetic fields more precisely and comprehensively than has ever been done in space before.

The sensors are arranged on each of the four MMS spacecraft according to Fig. 7.

3.1 Analog Flux-Gate and Digital Flux-Gate

The DC magnetometer measurements are provided by two flux-gate three-axis sensors, each at the end of 5-meter deployable booms, and associated electronics within the CEB. Provided by UCLA, each sensor consists of two magnetic cores, their housings and drive wire windings, 6 sense wire windings, 6 feedback wire windings, and two printed circuit boards mounted on an armature, which provides a framework for the components (see Russell et al. 2014, this issue, for a more complete discussion). The Analog Flux-Gate (AFG) has a somewhat different controller, provided also by UCLA, than the Digital Flux-Gate, which is

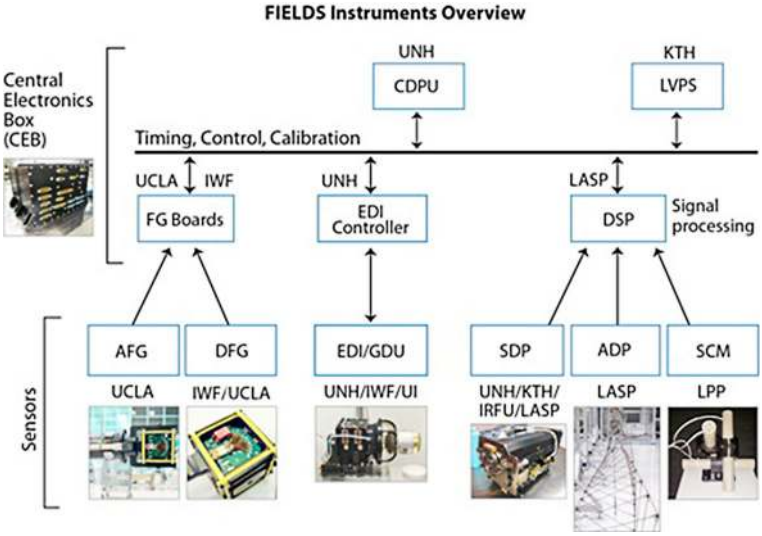

Fig. 6 FIELDS system configuration

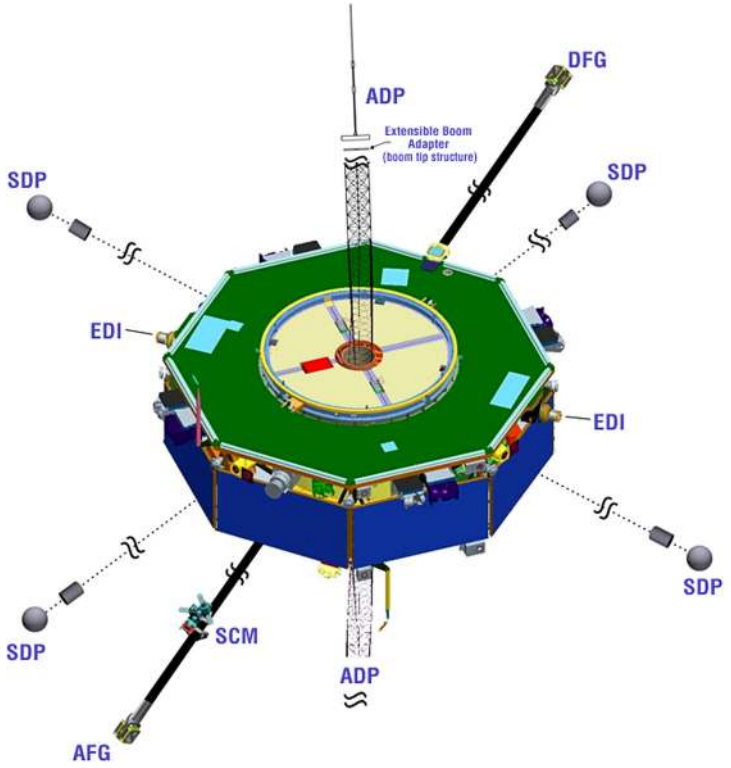

Fig. 7 FIELDS sensors on a MMS spacecraft

provided by IWF, but both magnetometers evolved to basically the same digital feedback design, although the DFG is implemented on a specially designed ASIC. Each controller produces a fixed 128 samples/s data stream to the Central Data Processing Unit (CDPU) within the CEB, which implements digital filters to reduce the sample rate if necessary due to telemetry restrictions. Two output ranges are available for both AFG and DFG, of $\sim$ 500 nT magnitude for low range to $\sim$ 8200/10500 nT (AFG/DFG), for high range. The ranges are commanded by the CDPU using an algorithm with hysteresis based on the data from the magnetometer controllers. Because of the key role of the magnetic field for reconnection studies, AFG and DFG provide fully redundant 3D data streams that are used both on-board the spacecraft by other instruments and also for ground processing. Extensive calibration and cross-calibration of the magnetometers was undertaken at the Technical University Braunschweig. An extensive magnetic cleanliness program for the MMS satellite system was supervised and validated by the magnetometer team. Also, timing calibrations were performed to determine the phase and gain curves versus frequency, as shown in Figs. 16 and 17. These calibration data show that both the AFG and DFG have the capability to measure the DC and low frequency component of the vector magnetic field over the full range of each magnetometer with a timing accuracy of better than 0.1 ms.

In order to reach the science objectives, the AFG and DFG magnetometers are also calibrated on orbit. The calibration procedures include comparison of the AFG and DFG gains and offsets across range changes, Earth-field comparisons, cross-calibration with

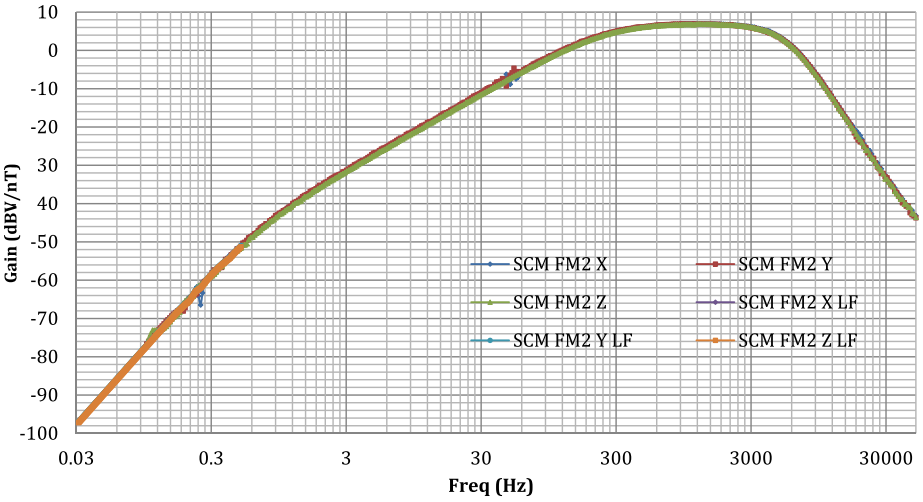

Fig. 8 FM2 SCM transfer function (gain) in dBV/nT from 30 mHz to 50 kHz

EDI, and inter-spacecraft calibration. More information can be found in Russell et al. (2014, this issue).

3.2 Search Coil Magnetometer

The SCM provides the three components of the magnetic fluctuations in the 1 Hz–6 kHz nominal frequency range, which is the imposed requirement. This range includes the hybrid wave and kinetic Alfvén wave frequency range as well as whistler mode waves (up to their cut off frequency equal to the electron gyrofrequency) and solitary waves. SCM consists of a triaxial induction search coil wound around a ferromagnetic core, mounted 4 meters out on the AFG boom, with the transfer function as measured for Flight Model 2 (FM2, Fig. 8). The noise equivalent magnetic induction (NEMI or sensitivity) of the search-coil antenna is less than or equal to 2 pT/sqrt (Hz) at 10 Hz, 0.3 pT/sqrt (Hz) at 100 Hz and 0.05 pT/sqrt (Hz) at 1 kHz. An in-flight calibration signal provided by DSP allows the verification of the SCM transfer function once per orbit.

The analog waveforms from a pre-amplifier are digitized and processed inside the DSP with a resolution at 1 kHz of 0.15 pT, and are telemetered as SCM 1, 2, and 3 as indicated in Table 1.

3.3 Spin-Plane Double Probe

The Spin-plane double probe instrument (SDP) measures the electric field in the spin plane by sensing the potential difference between four current-biased spherical titanium-nitride electrodes, each of diameter 8.0 cm at the end of 60-meter long wire booms. Together with the axial double probe instrument (ADP, described below), SDP measures the 3-D electric field with an accuracy of 0.5 mV/m over the frequency range from DC to 100 kHz. By means of a thin titanium wire, the spheres are held 1.75 m beyond the ends of a preamplifier which provides a low impedance, unity-gain signal of the sphere potential to electronics located at the base of each boom on the spacecraft, as seen in Fig. 7. The preamplifier outer casing is divided into an inner and outer "guard", which can each be biased at ± 10 V with respect to

the sphere. Current biasing to the sphere is routed also through the preamplifier. The unity gain signal is used to drive the outer conductors around the primary signal wire, thereby reducing the effective capacitance of the long wires in the boom, up to a frequency of about 300 Hz and voltages from −80 to +100 volts with respect to the spacecraft ground. Electric field components are produced by dividing the potential difference between opposite pairs of spheres (e.g., derived from $E12 = 0.0415 * (V1 - V2)$) by an effective antenna length. The factor of 0.0415 is the approximate electronic gain. The effective antenna length can be estimated by considering the field configuration of spheres just beyond the ends of long grounded wire booms immersed in a vacuum (Fahleson 1967). However, this length can vary slightly with plasma conditions and is determined in flight by comparison to known fields, such as those for co-rotation in the Earth's inner plasmasphere or those measured by EDI, as described below. There are also AC coupled versions of Eij (E12, E34, and E56) with higher gain, called Eij_AC. The actual voltages of the spheres, V1–V6, and their AC coupled versions (V1_AC and V2_AC) are also telemetered. Vx (V1 to V6) is also shared with other instruments on board, such as ASPOC, that request this data.

The voltage of a sphere in a plasma floats to a value such that the total net current to the sphere is zero. Thus, error currents, such as asymmetrical photo- or secondary emission from either the sphere itself or the surrounding electrodes and spacecraft drives error voltages in the values of Eij. Every effort has been made on MMS to reduce this effect. The spacecraft spin axis is tilted with respect to the sun so that neither the preamp nor the spacecraft will shadow the sphere. The spacecraft itself was subjected to a rigorous electrostatic cleanliness and symmetry program. The sphere coating is manufactured to be as uniform as possible. UV reflectance tests were performed to ensure optimum matches of coatings for sphere pairs. Biasing the sphere at the minimum of dV/dI (lowest effective resistance) is very effective in reducing voltage offsets driven by error current effects. The photoelectron cloud and variation of the spacecraft potential are reduced by active spacecraft potential control of the ASPOC instrument (Torkar et al. 2014, this issue). In-flight comparisons of the resulting field with EDI also serve to identify and eliminate the remaining errors, as described below.

Although ASPOC reduces both the magnitude and variation of the spacecraft potential, the gun energy spectrum is not a delta function, and thus small variations (~ 0.1 V) remain which are a function of the ambient electron flux to the spacecraft and the spheres. Analysis of these variations still allows an estimate of the local electron density, with assumptions about temperature, that are very useful in determining spatial variations of plasma conditions, predominantly the ambient density.

3.4 Axial Double Probe

The Axial Double Probe (ADP) instrument measures the electric field, DC to $\sim$ 100 kHz, along the spin axis of the MMS spacecraft with an accuracy of better than 1 mV/m. It uses the double probe technique by sensing the local plasma potential at two sensors separated by $\sim$ 29.2 m effective antenna length. The axial direction, which completes the vector electric field when combined with the SDP, has been the most challenging component of the DC electric field measurement. The physical antenna lengths are limited by mechanical difficulties, which include deployment of stiff booms while preserving spacecraft stability. The ADP baseline is nearly twice that of the Polar mission ($\sim$ 16 m) creating the longest axial baseline ever attempted for a DC electric field measurement.

The ADP on each of the spacecraft consists of two identical, 12.67 m graphite coilable booms (made by ATK space systems). A guard ring, 30.9 cm in diameter and 2.6 cm high, encircles the mounting plate at the end of the coilable boom. A second, smaller boom is

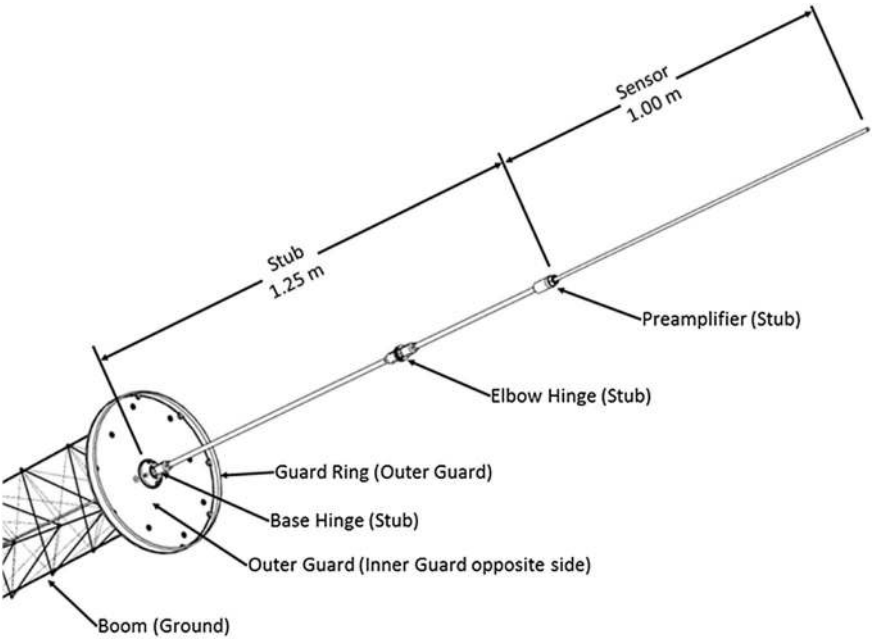

Fig. 9 Electrode configuration for the ADP sensor

mounted on the out-board end of each coilable boom. These 2.25 m booms (Fig. 9) are folded onto the top and bottom of the spacecraft for launch. The smaller outer boom is deployed soon after launch, followed several weeks later (after SDP is fully extended) by the deployment of the 12.67 m coiled boom. When deployed, the outer booms are comprised of (going away from the spacecraft) a 90° base hinge, a 0.78 m long by 1 cm diameter tube, a 180° hinge, a 0.43 m long by 0.95 cm diameter tube, a 5.6 cm long by 2.1 cm diameter preamplifier, and a 1 m long by 0.64 cm diameter sensor.

As done with the SDP, a significant effort has been made to assure a constant photo- and secondary electron current to the ADP sensors. All elements of the 2.25 m booms are cylindrical after deployment, including the hinges. The stubs, preamplifiers and sensors are coated with graphite-epoxy (DAG 213) to assure consistent surface properties as the spacecraft rotates. Equally important is the symmetry between the top and bottom sensors. The ADP booms are mounted to be symmetric about the spacecraft electrostatic plane, which is dominated by the spin-plane wire booms. As such, the lower boom (underside of the spacecraft in Fig. 7) is recessed into the spacecraft by ~ 0.1 m. The MMS spacecraft are to be oriented so that the ADP booms are within 5° of normal to the sun. A guard ring is placed at the base of the outer boom to shadow the top surface of the mounting plate. The guard ring is designed so that in the nominal attitude, the mounting plate is not exposed to the sun, assuring a nearly identical photo- and secondary electron environment near the two sensors.

As in the SDP, the ADP sensors are fed a bias current, often a significant fraction of the expected photoelectron current, to minimize the resistance between the plasma and the sensor. To further control the photoelectron environment, we control the surface potentials of (a) the guard ring, (b) the under side of the mounting plate, and (c) the hinges, stubs, and preamplifier housing. Each surface section can be set to ± 10 V with respect to the sensor's DC potential.

The ADP on MMS is expected to measure the DC electric field with an accuracy of ~ 1 mV/m, a resolution of 0.026 mV/m, and a range of $\sim \pm 1$ V/m in most of the plasma environments that MMS will encounter. Constant offsets between the booms will be removed by two methods: namely, minimizing $\mathbf{E} \cdot \mathbf{B}$ as measured by the double probe over long (> 20 s) periods and comparison with EDI electric field measurements. The spectral power density has a dynamic range from 4×10^{-16} $(\mathrm{V/m})^2/\mathrm{Hz}$ to 10^{-3} $(\mathrm{V/m})^2/\mathrm{Hz}$ at 10 kHz.

3.5 Electron Drift Instrument

EDI determines the electric and magnetic fields quite differently from all the sensors above. It is basically a geometric measurement for the electric field and a timing measurement for the magnetic field. As seen in Fig. 10, two electron beams are emitted in nearly opposite directions from two Gun-Detector Units (GDU) on opposite sides of each spacecraft. Each beam drifts in the $\mathbf{E} \times \mathbf{B}$ direction and, if properly directed, returns to the spacecraft after nearly one or more gyroperiods. If the drift-step ($\mathbf{d}$ = drift velocity, $\mathbf{v}_d$, times gyroperiod) is of the order of the baseline separation of the two GDU's, then the electric field is determined by triangulation as seen in Fig. 11. In this figure, the first GDU (G_1) emits a beam in the direction $\mathbf{V}_1$ that is detected by the opposite detector, D, and vice versa for G_2. The

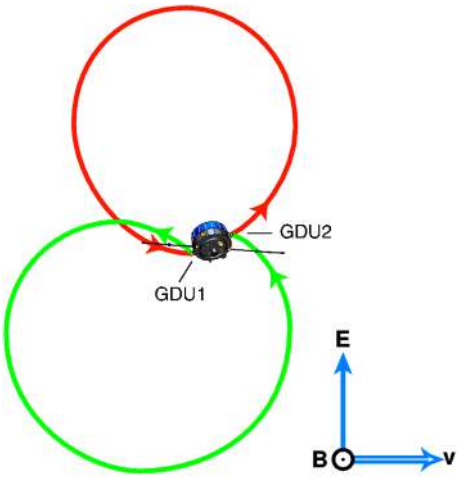

Fig. 10 Electron beam paths

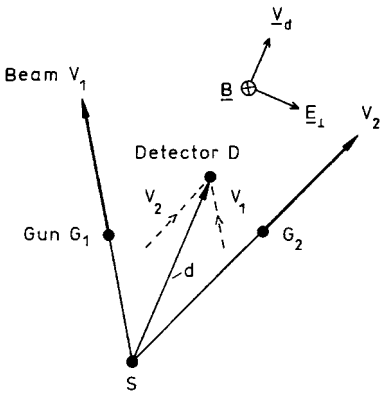

Fig. 11 Geometry of drift vector for EDI

drift step is the displacement of the intersection of the two beams (S) from the position of the detector. The actual geometry is slightly more complicated in that the detector for G_1 is located at G_2 and vice versa. The beams are pseudo-noise encoded so that the emitted electrons can be unambiguously detected in the presence of ambient electrons, and the time of flight of the beam can be determined. The difference of the time of flight of the two beams gives the magnitude of the drift step (which can be used in the "time-of-flight" mode when the drift step is large compared to the baseline) and the average of the two times gives the gyroperiod. From the gyroperiod, the magnitude of the magnetic field is determined, and from the directions of the successful beams, the direction of the magnetic field can be computed. The advantage of EDI over conventional electric and magnetic sensors is that the effects of the fields far from the spacecraft dominate the resulting vectors: electrostatic and noise magnetic fluctuations of the spacecraft have little effect when the gyroradius is of order kilometers, as is the case for MMS. But EDI also has a very slow time cadence for a full vector determination (of order 10 samples per sec) compared to AFG, DFG, SCM, SDP, and ADP. By combining multiple techniques, as described below, improved accuracy can be obtained with high time resolution. The requirements on FIELDS as a whole for an electric field accuracy of 0.5 mV/m and a magnetic field accuracy of 0.1 nT can thus be met. In order to detect the weak ($\sim$ 100 nA) electron beams emitted by the guns, the detector of EDI has very large geometric factor (order 0.01 cm^2 str) so that very fast sampling of ambient electrons is possible at a fixed energy and for a few directions. Thus, 0.5 or 1 keV electron fluxes can be determined in the "ambient" mode at 1024 samples per sec and very thin electron layers can be detected.

3.6 Central Electronics Box

The CEB directs all the activities of the FIELDS sensors and formats both housekeeping and science data for transmission to the CIDP and eventually to the downlink for ground processing. As diagrammed in Fig. 12, the operating system in CDPU (RTEMS) structures the flight software activities, and allows for command handling (CMD) by non-maskable interrupts (NMI) and memory error checking (EDAC). All magnetometer data comes from AFG

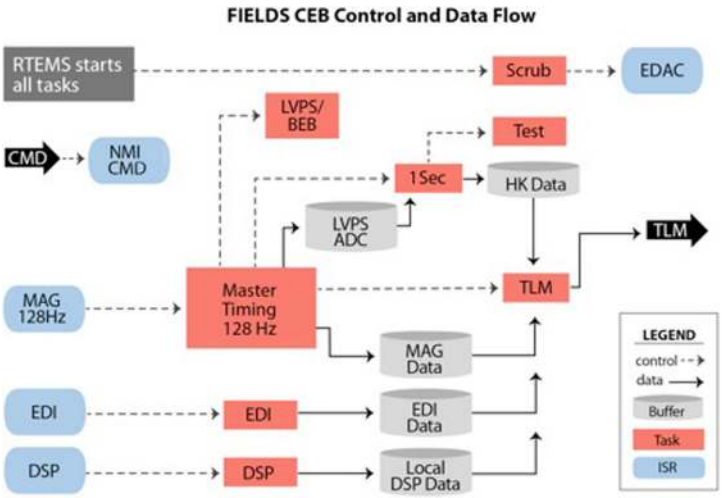

Fig. 12 Data procession path within the CEB

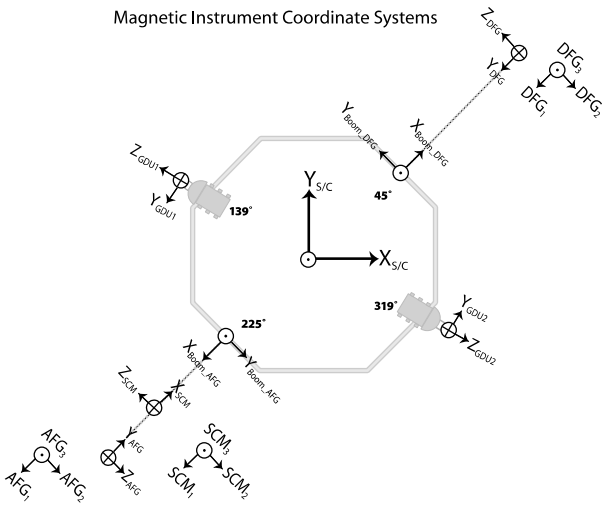

Fig. 13 Magnetic sensor system

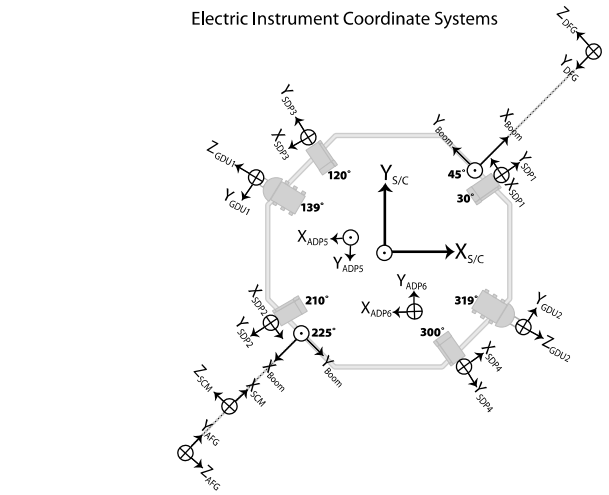

Fig. 14 Electric sensor system

and DFG as a continuous stream of 128 vectors per second. The CEB performs digital filtering on this data down to the commanded rate and also internal coordinate system rotation of the field components for use by FIELDS and other on-board instruments on MMS. The relevant coordinate systems are seen below (Figs. 13 and 14). The CEB directs the traffic of EDI and DSP data, and uses some of those data for internal calculations of the Trigger Data Numbers that are used in the ground algorithms to determined selection of BURST data. It also houses the Low Voltage Power Supply (LVPS) that controls all power distribution in FIELDS as well as the floating power supplies that drive both the SDP and ADP sensors.

Each of the FIELDS sensors can produce data over a large range of sampling rates, as seen in Table 1. In addition, all the DSP input channels (SCM, Vx, Eij, and Eij_AC) are used to produce spectral products over a time series of 1024 samples which are then averaged and sent down as a frequency spectrum (magnitude only). Ancillary data include in-flight calibration data for SDP, ADP, and SCM, and timing information in the housekeeping data. There are also specialized data products of the DSP that are short samples of all inputs at

Table 1 Possible sample rates for sensors within FIELDS

Quantity	Samples/s	
	Minimum	Maximum
AFG 1, 2, 3	8	128
DFG 1, 2, 3	8	128
DSP inputs		
SCM 1, 2, 3	0.5	16384
V1, V2, V3, V4, V5, V6	0.5	16384
E12, E34, E56	0.5	16384
E12AC, E34AC, E56AC	8	262144
V1AC, V2AC	8	262144
High speed burst data		
E12_AC, E34_AC, E56_AC	32768	262144
V1_AC, V2_AC	32768	262144
SCM 1, 2, 3	4	16384
EDI modes		
E Field mode: beam pairs	Variable	125
Ambient mode: flux samples	4	1024

very high rates, but only small duty cycles. These include the High Speed Burst channels (HSB-E and HSB-B) as well as the output of a Solitary Wave Detector algorithm.

Depending on the science questions to be addressed, a very large number of possible telemetry modes can be constructed by ground command. These are limited only by the total bit rate allocation for FIELDS seen in Table 3. As described in a companion paper on BURST mode (Fuselier et al. 2014, this issue), the CEB executes two basic modes, Slow and Fast Survey, and produces continuous data products that are always telemetered to the ground. In addition, very high data rate "BURST" products are produced only in Fast Survey mode and sent to the CIDP for storage. Only interesting intervals of this data are selected for ground transmission because there is not enough overall telemetry to accommodate BURST mode data over the full orbit. At launch, there are two modes for the BURST data: one for dayside reconnection studies in Phase 1 and one from the magnetotail studies in Phase 2. These default sampling modes, which can be changed or replaced in flight, are listed in Table 2 (nominal duty cycles for HSB are indicated as percentages).

The overall resource utilization of FIELDS is given below. The masses do not include those for spacecraft harness or magnetometer booms.

4 Timing

A central design goal of the FIELDS suite requires that its sensors are sampled on the same synchronous time base defined by the FIELDS independent clock. The FIELDS clock runs asynchronously to those in the CIDP and the spacecraft, thus requiring FIELDS time to be continually interpreted and cast in absolute terms. An absolute time reference is provided by the spacecraft GPS unit (the Navigator) and is distributed throughout the spacecraft. It consists of a one pulse per second (PPS) timing signal and the associated TAI time at the pulse. Correlation data contained within instrument housekeeping and instrument characteristics

Table 2 Nominal modes of FIELDS CEB

Quantity	Type	Components	Samples/s			
			Slow survey	Fast survey	Burst-phase 1	Burst-phase 2
EDI	Coded	Beam pair	∼16	∼16	∼125	∼125
AFG	Time series	3	8	16	128	128
DFG	Time series	3	8	16	128	128
DC-E	Time series	3	8	32	1024	8192
AC-E	Time series	3			8192	8192
DC-V	Time series	1 to 3	8	32	1024	8192
SCM	Time series	3	8	32	1024	8192
LFE	Spectra	1 or 3	0.0625	0.5		
MFE	Spectra	1 or 3	0.0625	0.5		
LFB	Spectra	1 or 3	0.0625	0.5		
HSB-E	Time series	3			65536@40 %	65536@10 %
HSB-B	Time series	3			16384@40 %	16484@10 %

Table 3 Resources for the FIELDS suite

Component	Power (W)		Mass (kg)
	Slow survey	Fast survey	
CEB	8.443	8.610	5.37
SDP	1.829	1.829	17.20
ADP	0.857	0.857	15.48
SCM	0.181	0.181	0.91
EDI	3.430	4.850	11.90
AFG	in CEB		0.74
DFG	in CEB		0.74
Totals	14.740	16.327	52.34
Data rates	Slow survey	Fast survey	Burst
kbits/s	2.36	7.93	843.61

are used to assimilate FIELDS time with the TAI information. The correction of FIELDS time into absolute terms is performed as part of ground processing. The FIELDS DSP and EDI components can be timed between themselves to better than 20 μs and to within 50 μs to the flux-gate magnetometers, which have a larger sample times of ∼ 8 ms. This greatly simplifies inter-sensor calculations of Poynting vectors, current sheets relative to electron fluxes seen by EDI, the algorithms that combine EDI, ADP, and SDP into one electric field record, and the algorithms that combine AFG, DFG, SCM, and EDI into one magnetic field record, as described below.

To assure this intra-sensor timing knowledge, an extensive suite of calibrations was conducted as part of the FIELDS Interference and Timing (FIT) campaign. This campaign consisted of two main parts: 1) an interference assessment to verify FIELDS self-compatibility and 2) a timing investigation to verify time tag accuracy, which is described here, and FIELDS-level frequency response of sensors. The timing investigation was divided into three specialized tests to address the specific workings of the electric field instruments (ADP

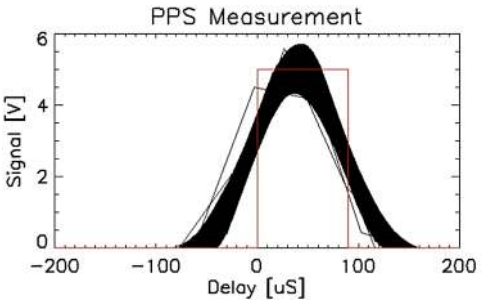

Fig. 15 Multiple PPS measurements taken by DSP SN12 with the idealized PPS pulse location (*red*)

Table 4 Time corrections applied to DSP data displayed in Fig. 14

PPS & Signal propagation delay description	Corrective value
PPS pulse transmission delay	23.7 μs
DSP expected analog delay	−60.6 μs
DSP ADC acquisition, sample and hold delay	−3.3 μs
DSP Mux delay: 3.8 μs ∗ (Channel-1). Zero for first sampled channel	+0 μs
DSP digital delay (16 kS/s sampling)	−183 μs
Total scalar timing adjustments	−223.2 μs
Frequency offset between FIELDS clock and PPS clock. Clock rate difference drifts throughtout testing due to temperature dependence. This effect is corrected for using information from FIELDS housekeeping packets	0 to 5 μs (variable)

and SDP), magnetometers (AFG, DFG, and SCM) and EDI. In each of these tests, sensor responses to calibrated, PPS-synchronous stimuli were recorded. The results were analyzed for time tag accuracy and precision and compared to the expected frequency response of the instrument.

4.1 DSP Timing

The ADP, SDP and SCM data time tags, which are provided by the DSP, were verified by the DSP direct-measurement of the PPS timing events. Known timing delays and advances from the PPS broadcast, data sampling, and coarse-fine time clock differences displace the time tag from the nominal value. The difference between the expected and measured PPS event time tags is a measure of the timing tagging accuracy. The jitter in the measured PPS event time tags is an estimate of the time tagging precision. Figure 15 shows 250 PPS measurements overlaid with the whole seconds removed and adjustments made for the known delays listed in Table 4. The 90-μs wide PPS pulse was not well-resolved by the 16 kS/s (60 μs) sampling of these tests. However, the center of the measurement still corresponds with the center of the PPS pulse. Since the rise of the PPS is what marks the start of a whole second, the corresponding location of the measured PPS was calculated by subtracting half the PPS pulse width (45 μs) from the time associated with the weighted center. This calculation was performed on each measured PPS event; the average and standard deviation of the resultant values are used to describe the distribution. DSP flight model #12 (FM12) measurements are shown here to have an unaccounted delay of -4.7 ± 2.0 μs, which is within the range that may be expected with jitters of up to 5 μs in the relative clocks.

Since the DSP time tags only the first sample of each data packet, the times of subsequent samples are assigned during ground processing, based on the channel sample rate and clock rate differences between the FIELDS and spacecraft (GPS) clocks. (Note that the clock rate difference is calculable, using the time tags from FIELDS housekeeping packets.) Stimulus applied at the top of a second is often placed in a packet with a time tag near the end of the previous second. This maximizes the time tagging error, so the values produced from this method are taken as the worst case.

4.2 AFG and DFG Timing

The AFG and DFG time tags are verified with known PPS-synchronous current stimulus, driven through test coils in a magnetically shielded environment and simultaneously measured by the sensors and a DSP channel. Differences in the sensor and DSP response to the stimulus, after adjusting for known timing advances and delays, are used to characterize the AFG and DFG time tags. The current generator test equipment provides arbitrary current and voltage stimuli with known timing relation to the PPS tone. The frequency responses of the magnetometers have been characterized with this current generator through two different methods.

Noise Cross Spectra: Pink and white noise signals were applied to the magnetic field sensors. The stimulus current was simultaneously recorded by a DSP channel, thus providing a time-accurate record of the stimulus applied to the sensors. Cross spectra calculations between the sensor-measured magnetic field and the independent DSP-measured reference provided the frequency response of the AFG, DFG and SCM sensors.

Sine Fit: A sine wave with known frequency and amplitude was applied to the test coil via the current generator. The sine signal was synchronized to the PPS tone with a well-defined phase relation. The sensor delay was determined as the difference between the phase of the measurement relative to the PPS via a numerical fit and the known phase relation of the stimulus.

Both methods were performed with the DFG and AFG sensors in the different permutations of range (high or low) and sampling rate (8, 16, 32, 64 and 128 Hz). DFG measurements were also performed in the different DEC (digital filter length, see Russell et al. 2014, this issue) modes (32 or 64), while AFG measurements were performed with both ADCs (A or B). The two measurement methods produce results within the range of expected values for all cases. Figure 16 shows the FM2 DFG noise cross spectrum results with 128 Hz sampling, low range and DEC32 modes. The delays for the x, y and z axes were 8.353, 8.303 and 8.321 ms, respectively. The expected value given known system delays is 8.308 ms $\pm$30 μs, which is in agreement with the noise cross spectrum measurement.

Table 5 shows the FM2 DFG sine fit results for time delays for the difference ranges at selected frequencies. The delays measured with the sine fit method are about $20-30$ μs larger than those measured with the noise—cross spectra method. The source of the discrepancy is not known, however both methods are within the range of the expected value.

Figure 17 shows the FM2 AFG noise cross spectrum results with 128 Hz sampling, low range and ADC-A. The delay for the x, y and z axes between 2–10 Hz was measured to be 11.425, 10.808 and 10.717 ms, respectively.

Table 6 shows the FM2 AFG sine fit results for the difference ranges at selected frequencies. Similar to the DFG results, the delays measured with the sine fit method are about 20–30 μs larger than those measured with the noise—cross spectra method. The source of the discrepancy is not known, however both methods verify the expected value well within the requirement measurement offsets.

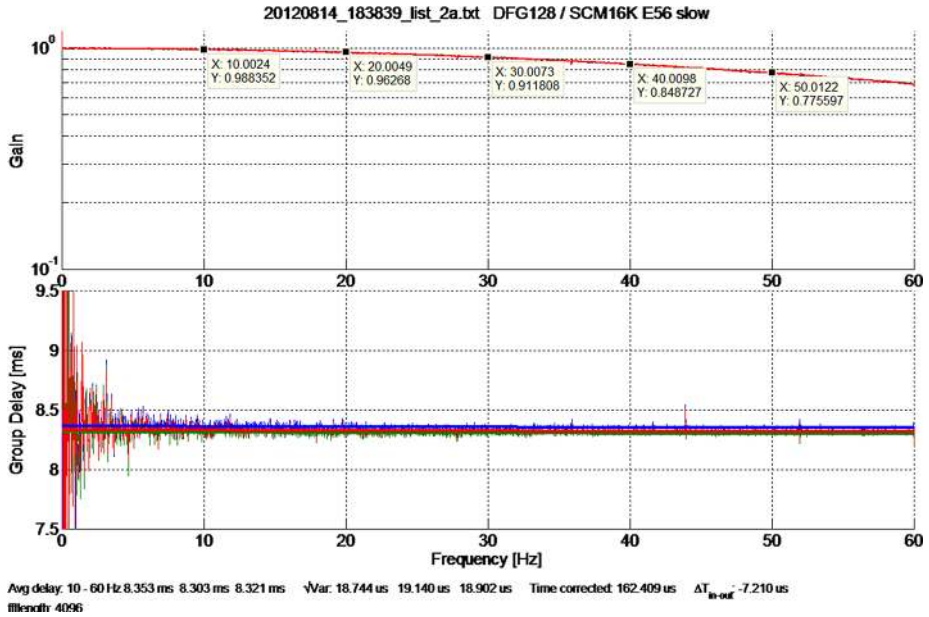

Fig. 16 Cross spectrum FM2 DFG 128 Hz, low range, DEC32 vs. DSP E56 16 kS/s

Table 5 Delay of FM2 DFG at various frequencies when measured with sine–sine fit method

Range	Freq. [Hz]	X [ms]	Y [ms]	Z [ms]
Low	0.1	8.410	8.358	8.378
Low	2	8.387	8.334	8.354
Low	8	8.374	8.322	8.342
Low	32	8.337	8.305	8.318
High	2	8.370	8.373	8.400

4.3 EDI Timing

EDI GDU time tags are verified with a PPS triggering of the EDI GDU test pulsers, which drives the particle counters within the GDU detectors at a known time. The resulting time-tagged sensor records are analyzed to calculate the time of the trigger. The difference between the calculated trigger time and the known time corresponding with the PPS trigger provides an accuracy estimate. The measurement is repeated 10 times per unit to estimate the precision of the time tagging and the measurement. Table 7 shows the results from the FM3 EDI-GDU test showing the time tags have an unaccounted delay of 0.41 ± 0.42 µs.

4.4 SCM Timing

The SCM timing test used the noise cross spectrum method with the current generator developed for the other magnetometers. The objective of the SCM timing test is to produce a comparison of the FIELDS-level amplitude response and delay results with the component-level calibration measurements done at Chambon-la-Foret with the SCM sensor and pre-amplifier.

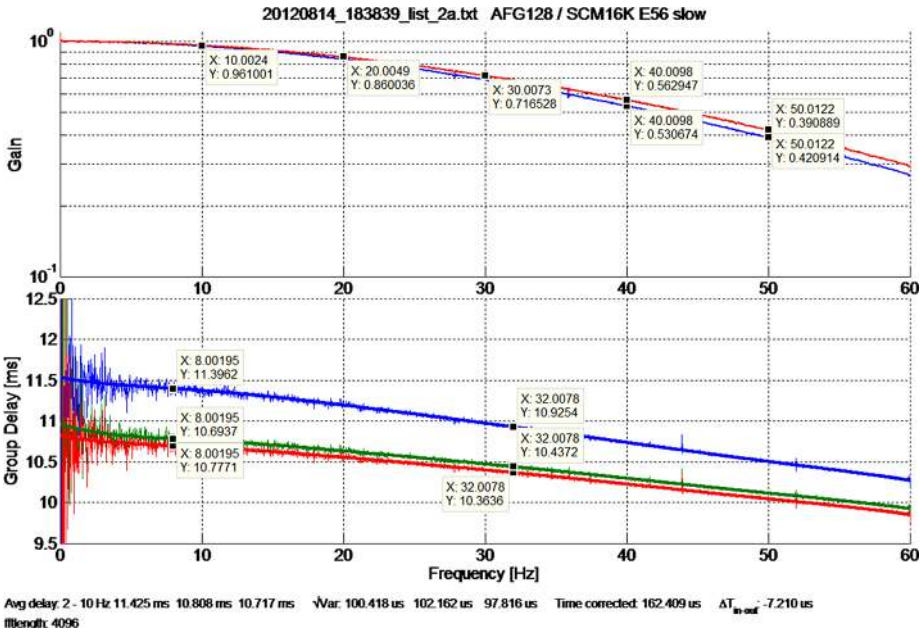

Fig. 17 Cross spectrum FM2 AFG 128 Hz, low range, ADC A vs. E56 16 kS/s; (*blue*) X, (*green*) Y, (*red*) Z

Table 6 Delay of FM2 AFG at various frequencies when measured with sine fit method

Range	Freq. [Hz]	X [ms]	Y [ms]	Z [ms]
Low	0.1	11.470	10.860	10.785
Low	2	11.449	10.817	10.728
Low	8	11.397	10.777	10.691
Low	32	10.916	10.446	10.358
High	2	11.452	10.819	10.732

Table 7 FIT test results for FM3 EDI-GDU

No.	EDI packet coarse time	EDI packet fine time (raw)	Transitional counts index	Transitional counts value	Full counts value	Predicted time of 1PPS	Nominal 1PPS	Deviation from full second [µs]
1	404	343922	673	172	1024	405.00000015	405	0.15
2	438	343906	673	156	1024	438.99999941	439	−0.59
3	474	343893	673	142	1024	474.99999976	475	−0.24
4	504	343883	673	132	1024	504.99999929	505	−0.71
5	529	343877	673	125	1023	529.99999985	530	−0.15
6	554	343871	673	119	1023	554.99999957	555	−0.43
7	579	343867	673	114	1023	580.00000034	580	0.34
8	604	343863	673	111	1024	604.99999932	605	−0.68
9	624	343861	673	109	1024	624.99999923	625	−0.77
10	644	343859	673	107	1023	644.99999902	645	−0.98
Result								0.41 ± 0.42

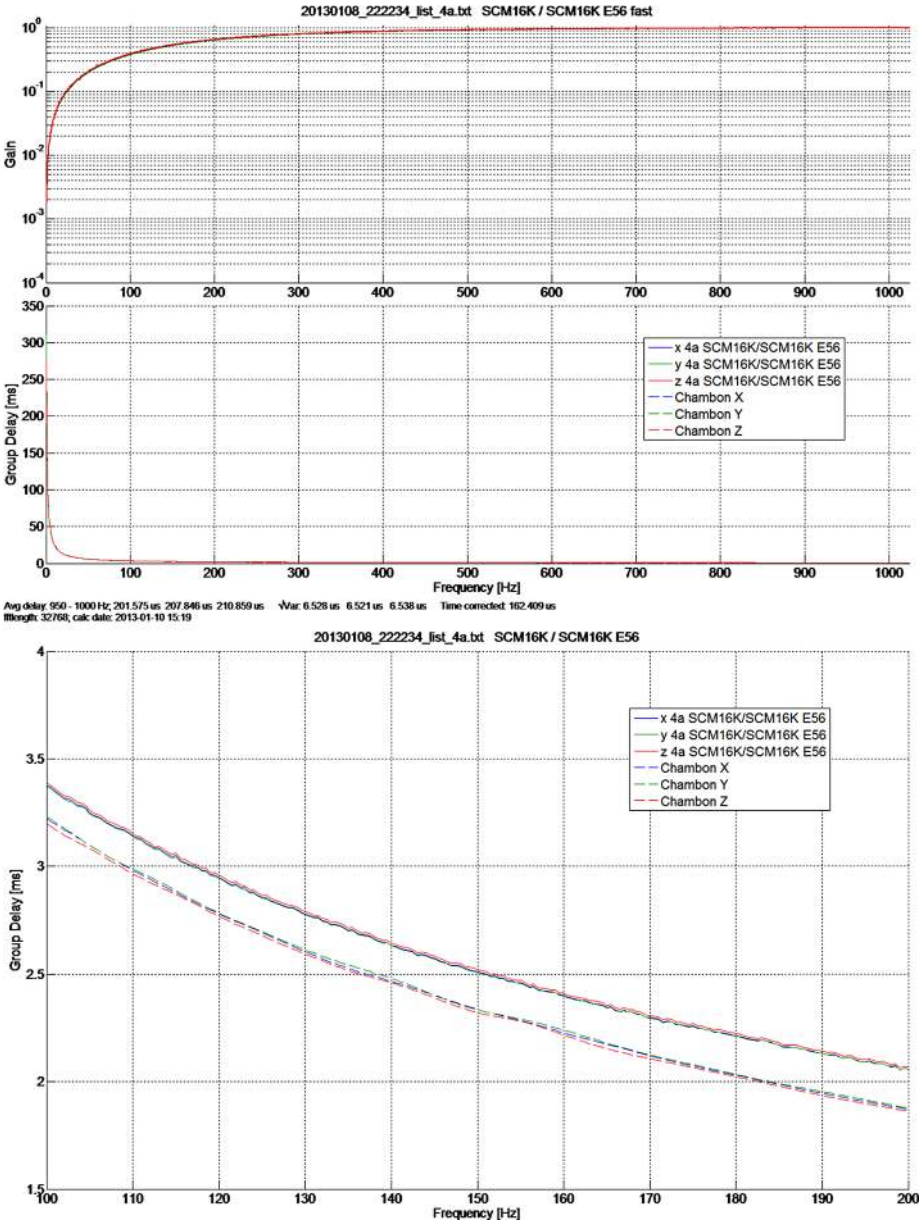

Fig. 18 Cross spectrum SCM 16 kS/s, DSP A vs. E56 16 kS/s; (*blue*) X, (*green*) Y, (*red*) Z

The difference between these two tests is the presence of the DSP, which contributes additional attenuation and delays due to analog and digital filters. The SCM noise cross-spectrum measurements were performed over different sampling rates (1, 8, and 16 kSamples/s) and for both of the redundant DSP boards. Figure 18 shows the FM3 results with 16 kS/s sampling and DSP-A plotted with the calibration results from Chambon-la-Foret. The zoom plot shows a 210 μs offset in the measured group delays. This additional delay of the digitized

Table 8 FIELDS routine data products

Sensor (s)	Description
FIELDS Quicklook products	
AFG	3-component B-field from Analog Flux Gate (AFG), to 16 vectors/s
DFG	3-component B-field from Digital Flux Gate (DFG), to 16 vectors/s
SDP-ADP	3-component E-field from Spin-plane Double Probe (SDP) and Axial Double Probe (ADP), to 32 samples/s
SDP-ADP	3-component Low Frequency (LF) electric spectra, 1–8000 Hz
SDP-ADP	3 sampled Medium Frequency (MF) electric spectra, 25–100 kHz
SCM	3-component LF magnetic spectra, 2–6000 Hz
EDI	Ambient electrons at two directions
FIELDS Level 2 products	
AFG	3-component B-field from Analog Flux Gate (AFG), to 128 vectors/s
DFG	3-component B-field from Digital Flux Gate (DFG), to 128 vectors/s
SDP-ADP	3-component E-field from Spin-plane Double Probe (SDP) and Axial Double Probe (ADP), to 8192 samples/s
SDP-ADP	3-component AC E-field from Spin-plane Double Probe (SDP) and Axial Double Probe (ADP), to 8192 samples/s
SDP-ADP	3-component high speed burst E-field from Spin-plane Double Probe (SDP) and Axial Double Probe (ADP), to 65536 samples/s
SDP-ADP	1 spacecraft potential sample from combination of ADP and SDP
SDP-ADP	3 sphere voltages from ADP and SDP
SDP-ADP	3-component Low Frequency (LF) electric spectra, 1–8000 Hz
SDP-ADP	3 sampled Medium Frequency (MF) electric spectra, 25–100 kHz
SCM	3-component AC B-field waveform from Search Coil Magnetometer (SCM)
SCM	3-component high speed AC B-field waveform, to 16384 samples/s
SCM	3-component LF magnetic spectra, 2–6000 Hz
EDI	Electric fields and drift velocity from Electron Drift Instrument (EDI)
EDI	Ambient electrons at two directions
FIELDS Level 2-plus products	
AFG-DFG-SCM	3-component combined B-field from all Mag sensors, to 1024 or greater vectors/s
SDP-ADP-EDI	3-component E-field from Spin-plane Double Probe (SDP) and Axial Double Probe (ADP) and Electron Drift Instrument (EDI), to 8192 samples/s

SCM data reflects the delay of the DSP channels, as referenced above in the DSP timing section.

5 Data Processing and Products

From data obtained in various modes, as seen in Table 2, programmed from possible data channels as in Table 1, ground processing produces a set of standard FIELDS data products that reside in the Science Data Center (SDC) and at the FIELDS Instrument Team Facility (ITF) at UNH.

Level 1 products for FIELDS are produced at the SDC from L0 data with software provided by the FIELDS team. For most of FIELDS data, Level 1 processing consists mostly of decompression of data and accurate time tagging for these data using the timing information

Table 9 In-flight calibration methods

Calibrated item	Comparator	Method	Frequency
AFG/DFG orthogonality	None	Spin plane quadrature, Spin-tone removal	Every orbit
AFG/DFG gains and offsets	Observatory AFG/DFG	Inter-observatory comparison	Monthly, or as needed
AFG/DFG gains	Spin-plane reference phase	Perigee pass analysis	Initial, quarterly or higher phase 1, 2
FG offsets	None	Variance analysis, Solar Wind	Yearly, as available
FG spin-axis offsets	EDI	Direction, TOF comparison	Weekly
SCM gains	AFG, DFG	Overlapping frequency band	Monthly
SCM gains, phase, offsets	None	Waveform analysis of cal signals	Daily
SDP, ADP gains	AFG, DFG	$-\mathbf{V}_{sc} \times \mathbf{B}$ perigee comparison	Initial, monthly phase 1, 2
SDP, ADP gains	FPI, HPCA	Solar Wind $-\mathbf{V} \times \mathbf{B}$ comparison	As available
SDP, ADP gains, offsets	EDI	Direct $\mathbf{E}_{perp}$ comparison	Continual, distinguishing different plasma regimes
SDP, ADP offsets	DFG, AFG	$\mathbf{E} \cdot \mathbf{B} = 0$ check	Quiet regions
SDP, ADP offsets	HPCA	$-\mathbf{V}_{O+} \times \mathbf{B}$ comparison	Lobe outflow regions
EDI MCP gains	None	Ambient response: MCP, pre-amp	Monthly

from sensors and the FIT tests described above. In some cases, there is a Level 1b data set where initial and tentative calibrations are applied for use in early processing.

The QuickLook and Level 2 products are produced initially using the best ground calibrations available for each sensor and then are combined in the manner that has been used in many previous missions such as Cluster, Polar, and THEMIS. QuickLook is available within 24 hours after the receipt of data; and Level 2, within 30 days. The FIELDS coordinate systems for this processing have been carefully co-aligned on the ground and are used for production of the first stage of this processing, and then rotated into the GSE coordinate system for science use.

For Level 2, the ground calibrations are augmented with an extensive set of on-orbit calibrations as listed in Table 9. During the mission, weekly conferences of both the magnetic field team and the electric field team on MMS will use these techniques to improve the overall accuracy of L2 data.

For MMS, the integrated FIELDS suite allows the combination of these products using new algorithms such as described below to achieve the accuracy needed for MMS. These products are listed as Level 2-Plus above and the production algorithms are described below.

FIELDS also contributes to the calculation of MMS Level 3 data products obtained from a combination of the data from different instruments. Seven parameters use FIELDS data: electron number density (from selected periods where the upper hybrid resonance frequency can be identified); Alfvén speed; $\mathbf{E} \times \mathbf{B}$ velocity; $\mathbf{E} + \mathbf{V}_e \times \mathbf{B}$; plasma beta; and energetic ion and electron anisotropy.

5.1 Combination Algorithms

To provide the environment for highly accurate magnetic field data from the combination of EDI, AFG, DFG, and SCM, the observatories must meet strict magnetic cleanliness require-

ments, as mentioned above. These requirements and how they were achieved and confirmed are described in Russell et al. (2014, this issue). The care taken to ensure that EDI, AFG, DFG and SCM are intercalibrated and accurately temporally referenced is described above. A complementary science objective is that the measurements across spacecraft be intercalibrated. For the fluxgate magnetometers, intercalibration is especially important for they are used to determine the currents that are flowing on the plasma boundaries. The intercalibration techniques for the magnetometers by themselves are described further in Russell et al. (2014, this issue). The procedures for combining data from the various FIELDS sensors are outlined here.

5.1.1 Magnetometer Spin-Axis Offset Determination

The magnetometer and EDI teams will use the EDI beam data, consisting of both electron gyro-periods and directions of the beam perpendicular to B, in an intensive collaborative effort to determine the spin axis offsets of the flux-gate (FG) magnetometers AFG and DFG (also used by SCM). In most previous satellite measurement sets, the generally used methods for in-flight determination of FG magnetometer spin axis offsets are based on the analysis of Alfvénic fluctuations in the solar wind. As MMS excursions into the solar wind will only be an exception in early mission phases, the spin-axis offsets will have to be determined by comparison with EDI data. Electron times-of-flight (TOFs) are inversely proportional to the strength of the ambient magnetic field. Furthermore, EDI beam firing directions (BDs) have to be perpendicular to that field for the beams to return to the spacecraft. Hence, comparison of both quantities, TOFs (T) and BDs ($\vec{D}$) to FG magnetic field measurements ($\vec{B}$) can yield spin axis offsets, if the FG data are sufficiently well calibrated for EDI to work at all. Here, we briefly describe the TOF and BD methods; more details can be found in Plaschke et al. (2014).

In the TOF method, the FG spin axis offsets are determined based on comparison between the FG magnetic field and the magnetic field magnitude deduced from EDI TOFs (Georgescu et al. 2006; Leinweber et al. 2012; Nakamura et al. 2014). As discussed in Nakamura et al. (2014), EDI TOFs may themselves be subject to offsets, which depend on individual sensor (GDU) and the mode of operation. Systematic TOF offsets can be obtained by comparison with $\vec{B}$ vectors that lie close to the spin plane, so that $|\vec{B}|$ is not much affected by spin axis offset uncertainties:

$$\delta T = T - \frac{k}{|\vec{B}|}$$

$$O_T = \text{median}(\delta T)$$

Here δT is the TOF offset determined from a pair of T and $\vec{B}$ measurements, k is a conversion factor between TOFs and magnetic field strengths, and O_T is the GDU/mode specific TOF offset, which the respective EDI measurements are to be adjusted with: $T_c = T - O_T$. As described in Plaschke et al. (2014), the median offsets O_T are determined from a large data set of measurements. Spin axis offset estimates are then obtained from adjusted TOFs by:

$$O_{SA} = B_{SA} - \text{sign}(B_{SA})\sqrt{\frac{k^2}{T_c^2} - B_{SP}^2}$$

Here, the indices SA and SP denote spin axis and spin plane components, respectively.

In the BD method, the FG spin axis offsets are determined based on the perpendicularity of BD and magnetic field. Ideally, the angle α between $\vec{D}$ and $\vec{B}$ is 90°. The BD method is not affected by TOF offsets, but requires accurate transformations of $\vec{D}$ and $\vec{B}$ into a common, spacecraft-fixed, and spin aligned coordinate system. The GDU-specific transformations can be adjusted by minimization of $(\alpha - 90°)^2$, where the angles α are computed from near-spin-plane BDs $\vec{D}$ (least affected by FG spin axis offsets). FG spin axis offset estimates are then obtained by:

$$O_{SA} = \frac{\vec{B} \cdot \vec{D}}{D_{SA}}$$

The TOF and BD methods for spin axis offset determination are complementary with respect to the directions of $\vec{D}$ and $\vec{B}$. The TOFs are compared to FG measured $|\vec{B}|$ values, which are most affected by offsets if $\vec{B}$ points in spin axis direction. Instead, BDs are most sensitive to changes in offsets if directed toward the spin axis. These conditions are mutually exclusive as $\vec{D} \perp \vec{B}$. Consequently, by combining these two methods taking into account the different sensitivity dependence to the field conditions, a comprehensive scheme of offset determination will be performed.

5.1.2 AFG-DFG-SCM Combination

Electron diffusion regions and thin current sheets pass over the MMS spacecraft in time intervals of 0.5 to 2 seconds because a typical region size of 5 to 20 km moves with a boundary speed of 10 to 100 km/sec. See, for example, Fig. 2. The frequency range of 0.5 to 20 Hz transitions from a low-frequency boundary where the SCM has little signal to a high-frequency one where the FG loses its ability to accurately track fields that vary this fast. Thus, on MMS, it is critical to have algorithms to combine these two measurements in this overlapping frequency band into one accurate data series. We use two methods: one time-domain and one frequency domain.

Both methods rely on preprocessing of the data by standard methods, which includes time tagging, offset and maximum gain correction, orthogonalization and transformation to a common coordinate system for both FG and SCM signals. For this purpose data from ground and inflight calibration are used, including also data from EDI.

The frequency domain algorithm applies a Tukey window to the data, which has unity gain at the central half of the data. Each data set is then Fourier transformed and corrected with the amplitude and phase responses found during ground individual and cross calibration. At this point, the spectra are compared for consistency over the overlap frequency range from 0.2 Hz to 64 Hz to assure correct processing.

The two complex frequency spectra are now merged as follows. Below a lower transition frequency ($\sim$ 0.5 Hz, well above the spin frequency), we use the FG data exclusively. Above 16 Hz, we use the SCM data exclusively. Between these two frequencies, we use a weighted average of the two, with the weight determined by the amount that the individual power spectra exceeds the determined noise power threshold. These thresholds are determined by a statistical histogram of power at various frequencies, with data taken over selected quiet intervals. This new combined spectrum is then reverse Fourier transformed, window corrected, and then rotated into the spacecraft coordinate system. Now, only the central half of this time interval is used for the final data. At the beginning and end segments of any analysis interval, the first quarter and last quarter of those respective segments are used as well.

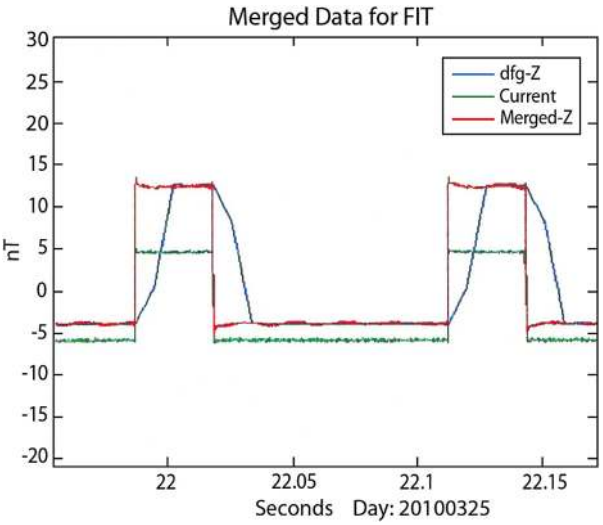

Fig. 19 Results of FG/SCM combination algorithm

The time domain algorithm is based on adapting compensation filters in a way that the total response of each instrument has a selected low-pass (FG) or high-pass (SCM) characteristic. Those filters are chosen such that their summed response is close to unity gain and linear phase within the whole band of interest of the combined data product. The crossover frequency (cutoff of both filters) is a parameter that can be chosen dependent on noise power comparison of both instruments.

The combined data product can then be calculated by converting both signals to a common sampling base, applying the relevant filters and merging the signals. To minimize the influence of filtering on short bursts of higher frequency, the previous low frequency data is used to preload the filters.

In principle both are approaching the same problem with different focus. The frequency domain algorithm is concentrated on getting the minimum noise power within the combined signal, whereas the time domain algorithm is focused on creating a signal without side-effects (pre- and post-echo) caused by signal processing, but at the price of higher noise.

The frequency domain algorithm has already been applied to both Cluster test data and calibration data from the MMS FIT tests, as seen in Fig. 19, where DFG and SCM data have been combined.

Although the test configuration did not allow proper coordinate system rotations, all the timing delays described above and the measured transfer functions were used to implement the combination procedure to test how well MMS resolves sharp transitions of the magnetic field. The close correspondence of the driving field current (green trace) and the merged data show that sharp structures with time durations well below 5 ms can be reconstructed.

Further investigations of data gained during the FIT tests are still ongoing to get better models for the frequency properties of the instruments.

5.1.3 SDP-ADP-EDI

Using all three axes of ADP/SDP, a full vector electric field can be constructed at the full sample rate of the DSP (up to 16384 samples/s, or higher if need be). However, the Double-probe method is susceptible to well-known offsets due to electric fields induced by photoemission charges and the resulting electron cloud, and to wake effects of the satellite as

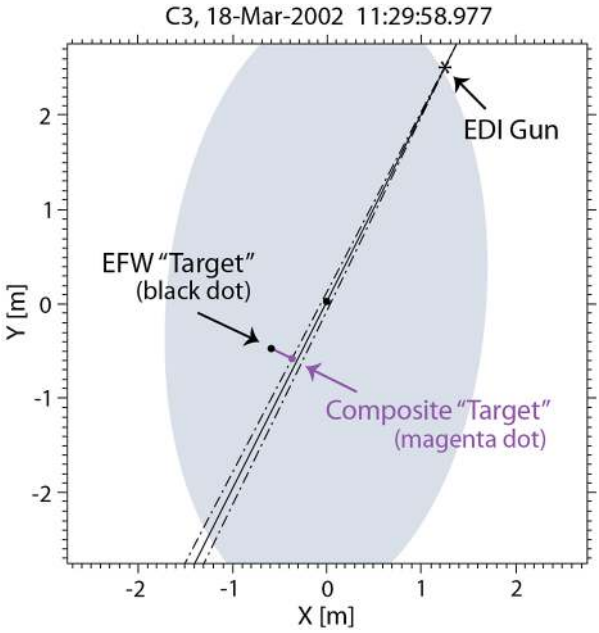

Fig. 20 Analysis of $\mathbf{E} \times \mathbf{B}$ drift in the Bperp plane

it moves through the ambient plasma. Due to the fact that the electron beam spends most of its time well away from the spacecraft, EDI is not affected by these offsets, but is able to produce a field value only perpendicular to the magnetic field at about 10 samples/s. To achieve the 0.3 mV/m accuracy, which is the MMS goal, we must combine these measurements to produce an accurate high-rate field measurement and to estimate the error in that measurement. A new algorithm, called BESTARG2, has been developed to do this.

For the first step, the field values from ADP/SDP and EDI are compared to remove the well-known sun-aligned (or GSE-X) component offset in the DP measurement that results from the local photoelectron cloud. A smoothing algorithm produces a slowly varying value for this offset and then removes it from the DP component. Then the DP 3D field value closest to a *single* EDI beam is projected into the plane perpendicular to B and used to produce a drift step "target" such as EDI measures (drift step $\mathbf{d}$ = drift velocity, $\mathbf{v}_d$, times gyroperiod, see Fig. 11). As the spacecraft turns, the GDU's move on the boundary of the shaded ellipse in the Bperp plane. Level 2 data from EDI uses multiple beams from both GDU's to determine the drift step, as seen in Fig. 11 above, but by using every single beam, BESTARG2 is able to compare fields on a much faster time cadence. The true target must lie somewhere on the beam line, and if there were simultaneously two EDI beams, they would be at the intersection of the two beams. The composite field value is determined by displacing the DP drift step by the minimum amount to move it onto the single beam line, and the error is estimated by the length of that displacement (see Fig. 20).

The BESTARG2 analysis was performed on several intervals of Cluster data using EFW (the equivalent to SDP) and EDI when the magnetic field was mostly perpendicular to the spin plane so that both techniques were measuring in the Bperp plane. The results are given in Fig. 21. Here the black trace in the upper panel is the initially corrected L2 data from the double probes. The above algorithm then produces the magenta trace in the middle panel. The estimated resulting error is plotted in the lower panel, showing that errors of less than 0.5 mV/m are possible.

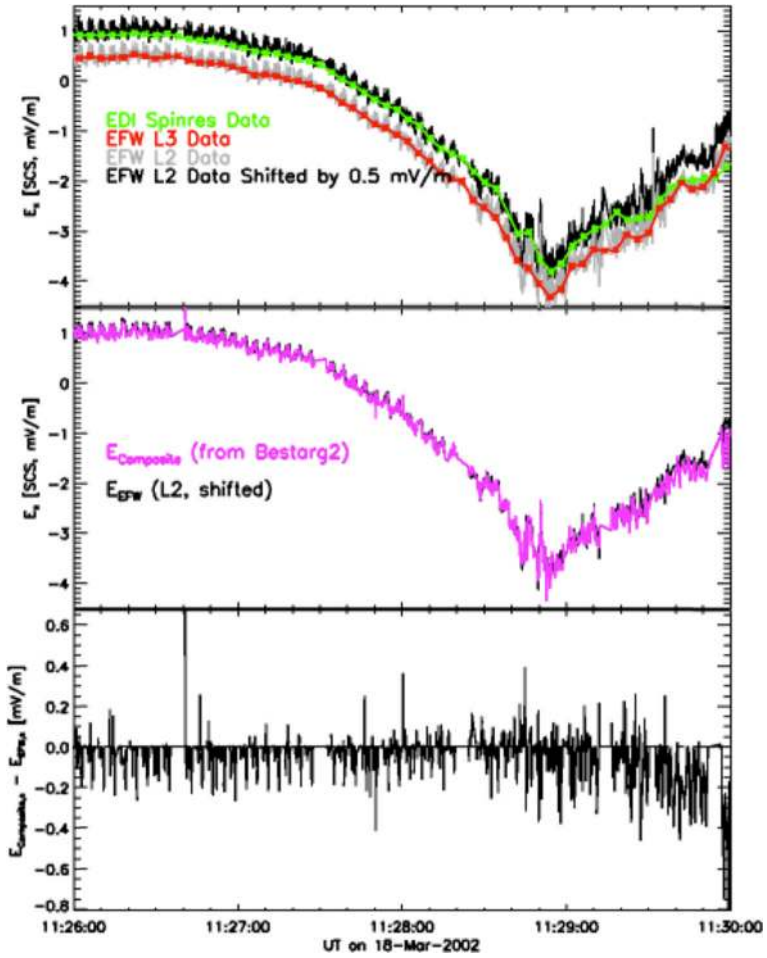

Fig. 21 Results of combining EDI with EFW on Cluster using BESTARG2

During the MMS mission, a study of the resulting errors, taking into account bias levels on the ADP/SDP and plasma environmental conditions may lead to a better understanding of the origin of the error and its reduction by different biasing schemes on the DP electrodes and/or better beam detection schemes on EDI.

6 Conclusion

With its highly integrated and inter-calibrated suite of sensors, the FIELDS instrumentation is well constructed to fulfill its requirements. The precise measurement of the fully 3D electric and magnetic fields will allow MMS to map magnetic topology and resolve structures of the electron and ion diffusion regions; determine the motion and orientation of boundaries such as the magnetopause and the magnetotail current sheets; establish mass flow rates across magnetopause during reconnection; and determine the breaking of the frozen-in flow velocity and the divergence of Poynting flux across the reconnection boundary. Combining

all the capabilities of the FIELDS suite with those of the particle instrumentation on four versatile satellites, MMS provides a mission to advance significantly our understanding of magnetic reconnection.

Acknowledgements Development of the FIELDS instrumentation suite has been the joint effort of many groups within the authors' institutions over the last 15 years. We acknowledge here generous support by the Space Science Center and the EOS Institute at UNH and the many staff members who gave a great part of their careers in the development of MMS. We wish to thank the generous assistance of technical and management staff at NASA GSFC and at SwRI, in particular W.C. Gibson and R.K. Black for managing the entire SMART instrument suite. FIELDS was developed under NASA MMS contract NNG04EB99C via the SwRI subcontract to UNH.

References

M. Andre, A. Vaivads, S.C. Buchert, A.N. Fazakerley, A. Lahiff, Thin electron-scale layers at the magnetopause. Geophys. Res. Lett. **31**, L03803 (2004). doi:10.1029/2003GL018137

T.G. Cowling, Solar electrodynamics, in *The Sun*, ed. by G.P. Kuiper (University of Chicago Press, Chicago, 1953), pp. 532–591

J.F. Drake, Particle heating and acceleration in magnetic reconnection, in *Magnetic Reconnection: An Interdisciplinary Workshop*, Yosemite, CA (2010)

J.W. Dungey, Conditions for the occurrence of electrical discharges in astrophysical systems. Philos. Mag. **44**, 725–739 (1953)

J.W. Dungey, Interplanetary magnetic field and the auroral zones. Phys. Rev. Lett. **6**, 47–48 (1961)

J. Egedal, W. Daughton, A. Le, Large-scale electron acceleration by parallel electric fields during magnetic reconnection. Nat. Phys. (2012). doi:10.1038/NPHYS2249

U. Fahleson, Theory of electric field measurements conducted in the magnetosphere with electric probes. Space Sci. Rev. **7**, 238–262 (1967)

S.A. Fuselier, W.S. Lewis, C. Schiff, R. Ergun, J.L. Burch, S.M. Petrinec, K.J. Trattner, Magnetospheric multiscale science mission profile and operations. Space Sci. Rev. (2014, this issue). doi:10.1007/s11214-014-0087-x

E. Georgescu, K.-H. Fornacon, U. Auster, A. Balogh, C. Carr, M. Chutter, M. Dunlop, M. Förster, K.-H. Glassmeier, J. Gloag, G. Paschmann, J. Quinn, R. Torbert, Use of EDI time-of-flight data for FGM calibration check on Cluster, in *Proceedings of the Cluster and Double Star Symposium 5th Anniversary of Cluster in Space* (ESTEC, Noordwijk, 2005)

E. Georgescu, H. Vaith, K.-H. Fornacon, U. Auster, A. Balogh, C. Carr, M. Chutter, M. Dunlop, M. Foerster, K.-H. Glassmeier, J. Gloag, G. Paschmann, J. Quinn, R. Torbert, Use of EDI time-of-flight data for FGM calibration check on Cluster, in *Cluster and Double Star Symposium*. ESA Special Publ., vol. 598 (2006)

R.G. Giovanelli, A theory of chromospheric flares. Nature **158**, 81–82 (1946)

M. Hesse, N. Aunai, J. Birn, P. Cassak, R.E. Denton, J.F. Drake, T. Gombosi, M. Hoshino, W. Matthaeus, D. Sibeck, S. Zenitani, Theory and modeling for the magnetospheric multiscale mission. Space Sci. Rev. (2014, this issue). doi:10.1007/s11214-014-0078-y

F. Hoyle, Magnetic storms and aurorae, in *Some Recent Researches in Solar Physics* (Cambridge University Press, Cambridge, 1949), pp. 92, 102–104

H.K. Leinweber, C.T. Russell, K. Torkar, In-flight calibration of the spin axis offset of a fluxgate magnetometer with an electron drift instrument. Meas. Sci. Technol. **23**, 105003 (2012). doi:10.1088/0957-0233/23/10/105003

F.S. Mozer, S.D. Bale, T.D. Phan, Evidence of diffusion regions at a subsolar magnetopause crossing. Phys. Rev. Lett. **89**, 015002 (2002)

R. Nakamura, F. Plaschke, R. Teubenbacher, L. Giner, W. Baumjohann, W. Magnes, M. Steller, R.B. Torbert, H. Vaith, M. Chutter, K.-H. Fornacon, K.-H. Glassmeier, C. Carr, Interinstrument calibration using magnetic field data from the flux-gate magnetometer (FGM) and electron drift instrument (EDI) onboard Cluster. Geosci. Instrum. Method. Data Syst. **3**, 1–11 (2014). doi:10.5194/gi-3-1-2014

E.N. Parker, Sweet's mechanism for merging magnetic fields in conducting fluids. J. Geophys. Res. **62**, 509–520 (1957)

E.N. Parker, Astrophys. J. Suppl. **77** (8), 177 (1963)

H.E. Petschek, Magnetic field annihilation, in *AAS–NASA Symposium on the Physics of Solar Flares, NASA SP-50*, Washington, DC ed. by W.N. Hess, (1964), pp. 425–439

F. Plaschke, R. Nakamura, H.K. Leinweber, M. Chutter, H. Vaith, W. Baumjohann, M. Steller, W. Magnes, Flux-gate magnetometer spin axis offset calibration using the election drift instrument. Meas. Sci. Technol. (2014, submitted)

P.L. Pritchett, F.S. Mozer, Asymmetric magnetic reconnection in the presence of a guide field. J. Geophys. Res. **114**, JA014343 (2009)

C.T. Russell, B. Anderson, W. Baumjohann, K. Bromund, D. Dearborn, G. Le, H. Leinweber, D. Leneman, W. Magnus, J.D. Means, M. Moldwin, R. Nakamura, D. Pierce, K. Rowe, J.A. Slavin, R.J. Strangeway, R. Torbert, C. Hagen, I. Jernej, A. Valavanoglou, I. Richter, The magnetospheric multiscale magnetometers. Space Sci. Rev. (2014, this issue). doi:10.1007/s11214-014-0057-3

B.U.O. Sonnerup, Reconnection of magnetic fields, in *Solar Terrestrial Physics: Present and Future*. NASA Ref. Pub., vol. 1120 (1984). Chap. 1

K. Torkar, R. Nakamura, M. Tajmar, C. Scharlemann, H. Jeszenszky, G. Laky, G. Fremuth, C.P. Escoubet, K. Svenes, Active spacecraft potential control investigation. Space Sci. Rev. (2014, this issue). doi:10.1007/s11214-014-0049-3